



ORIGINAL PAPER

Xuzhi Du · Anning Wei · Yuhao Fang · Zhigang Yang ·  
Daniel Wei · Chao-Hsin Lin · Zheyang Jin

## The effect of bend angle on pressure drop and flow behavior in a corrugated duct

Received: 14 February 2020 / Revised: 21 April 2020 / Published online: 28 June 2020  
© Springer-Verlag GmbH Austria, part of Springer Nature 2020

**Abstract** In the present study, the effect of bend angle on pressure drop and flow behavior in a small-diameter corrugated duct is numerically investigated and experimentally validated under a fully developed flow condition. The large eddy simulation, together with the proper orthogonal decomposition (POD) method, is employed to study the pressure drop, mean flow pattern, and unsteady flow evolution for a corrugated duct with various bend angles. The results show that the pressure drop exhibits a monotonic increase with increasing bend angle. Specifically, as the bend angle increases from  $0^\circ$  to  $90^\circ$ , the pressure drop of the corrugated duct experiences a striking increase of about 43%. Accordingly, a larger bend angle is found to induce the occurrence of stronger Dean cells or larger swirl intensity downstream the duct bend. Meanwhile, as for larger bend angles, the main turbulent properties of the Dean cells could be, to some extent, governed by the first few POD modes, which appear to be featured with one or a few large-scale vortices. Generally, the larger bend angle causes stronger

**Electronic supplementary material** The online version of this article (<https://doi.org/10.1007/s00707-020-02716-5>) contains supplementary material, which is available to authorized users.

X. Du · Y. Fang · Z. Yang · Z. Jin (✉)  
Shanghai Automotive Wind Tunnel Center, Tongji University, Shanghai 201804, China  
E-mail: zheyangjin@tongji.edu.cn

X. Du  
E-mail: 2013xuzhi\_du@tongji.edu.cn

X. Du · Y. Fang · Z. Yang · Z. Jin  
Shanghai Key Lab of Vehicle Aerodynamics and Vehicle Thermal Management Systems, Shanghai 201804, China

A. Wei · Z. Jin  
School of Aerospace Engineering and Applied Mechanics, Tongji University, Shanghai 200092, China

Z. Yang  
Beijing Aeronautical Science and Technology Research Institute, Beijing 102211, China

D. Wei  
Boeing Research & Technology - China, Beijing 100027, China

C.-H. Lin  
Boeing Commercial Airplanes, Seattle, WA 98124, USA

Z. Jin  
Key Laboratory of Icing and Anti/De-icing of Aircraft, China Aerodynamics Research and Development Center, Mianyang 621000, Sichuan, China

swirl intensity and wave-like structures, thus rendering severer pressure drop or larger pressure loss coefficient in the corrugated duct.

### List of symbols

$a_j(t)$	Temporal coefficients
$A$	Area
$C_D$	Cell-centered values of the coefficient
$C_{P,sta}$	Nondimensional form of pressure drop
$C_{P,tot}$	Total pressure loss coefficient
$\bar{C}_{P,tot}$	Overall mass averaged total pressure loss coefficient
$C_s$	Smagorinsky constant
$D$	Effective diameter of corrugated duct
$L$	Length of corrugated duct
$\dot{m}$	Mass flow
$N$	POD mode number
$P$	Instantaneous pressure
$P_{sta}$	Static pressure
$P_t$	Local total pressure
$P_{t0}$	Total pressure at the inlet
$r$	Variable of integration
$R$	Effective radius of corrugated duct
$\mathbf{R}$	Covariance matrix
$R_c$	Bend centerline radius
$Re$	Reynolds number
$\bar{S}_{ij}$	Rate of strain tensor
$Sw$	Swirl number
$t$	Time
$t^*$	Nondimensional time
$u$	$x$ Component of instantaneous velocity
$u_i$	$i$ Component of instantaneous velocity
$u_{in}$	In-plane velocity
$u_j$	$j$ Component of instantaneous velocity
$u_n$	Normal velocity
$u(t)$	Fluctuating velocity component
$\bar{u}(\xi)$	Mean velocity field
$u(\xi, t)$	Instantaneous velocity field of snapshots
$U$	Velocity
$\mathbf{U}$	Matrix form of snapshots' data
$U_{ax}$	Axial velocity component
$U_\theta$	Tangential velocity component
$v$	Instantaneous velocity in $y$ direction
$V$	Volume of the cell
$w$	Instantaneous velocity in $z$ direction
$W$	Mean streamwise velocity
$W_b$	Inlet velocity
$x$	Coordinate axis
$x_i$	$i$ Component of coordinate axis
$x_j$	$j$ Component of coordinate axis
$y$	Coordinate axis
$y^+$	Nondimensional distance from the wall
$z$	Coordinate axis

### Greek symbols

$\beta$	Bend angle ( $^\circ$ )
---------	-------------------------

$\gamma$	Bend curvature ratio
$\delta_{ij}$	Kronecker delta
$\Delta$	Filter width
$\Delta P$	Pressure drop
$\Delta t$	Time step
$\lambda_j$	Eigenvalues
$\Lambda$	Matrix form of eigenvalues
$\mu_t$	Subgrid-scale eddy viscosity
$\nu$	Kinetic dynamic viscosity
$\rho$	Air density
$\tau_{kk}$	Isotropic part of the subgrid-scale stresses
$\tau_{ij}$	Subgrid-scale stress
$\phi_j$	POD modes
$\Phi$	Matrix form of POD modes
$\psi_j$	Eigenvectors
$\Psi$	Matrix form of eigenvectors
$\omega_Z$	Streamwise vorticity

### Abbreviations

ACCA	Air Conditioning Contractors of America
ASHRAE	American Society of Heating, Refrigerating and Air-Conditioning Engineers
CFD	Computational Fluid Dynamics
CFL	Courant–Friedrichs–Lewy
ESP	Electronically scanned pressure
FS	Full scale
LES	Large eddy simulation
POD	Proper orthogonal decomposition
RANS	Reynolds-averaged Navier–Stokes
SGS	Subgrid-scale
SIMPLE	Semi-implicit method for pressure-linked equations
TKE	Turbulent kinetic energy

## 1 Introduction

Corrugated ducts are widely used within building heating, ventilation, and air-conditioning (HVAC) systems due to their potential flexible nature, ease of installation, low cost, sound attenuation, preinstalled duct insulation [1–3], etc. However, during the widespread usage of corrugated ductwork, the high pressure drop/loss within the corrugated duct seems to be one of the key culprits affecting the efficiency of the whole HVAC system [4,5]. Generally, this high pressure drop phenomenon is deemed to be caused by two major aspects: one is the intrinsic roughness of the corrugated wall; the other is that corrugated ducts can be inevitably forced to make bends during most installation scenarios of the HVAC system.

Over the past few decades, researchers have tried to study the pressure loss within straight run corrugated ducts, especially for compressed ones which typically increases the roughness and thus the total pressure losses of the ducts. Kokayko et al. [6] conducted a pioneering-experimental research on static pressure loss in straight corrugated ducts with various diameters (i.e., 6, 8, 10, 12 in.) and compressions. The results showed that the pressure losses associated with the relaxed corrugated ducts were much greater than the taut ones; meanwhile, the pressure losses of the 10% compression ducts were 35% to 40% higher than the maximum stretched ones. Abushakra et al. [7] experimentally investigated the effects of compression on static pressure loss in nonmetallic corrugated ducts. Their results indicated that the actual static pressure losses could be much higher than the calculated values based on ASHRAE 2009 [8]; meanwhile, the static pressure losses in corrugated ducts derived from the Air Conditioning Contractors of America (ACCA) Manual D [9] were 17% to 24% lower than the measured values. Following that, Weaver and Culp [1] performed an experimental study on static pressure loss in nonmetallic corrugated ducts with a wider range of compressions. Their results revealed a basic correlation with the previous work proposed by Abushakra et al. [7]. Moreover, Ugursal and Culp [10] comparatively studied the

pressure drop of compressed corrugated ducts by steady CFD simulations and experimental tests. The results suggested that the CFD model could simulate the pressure drops within 5% to 10% of the measured values for corrugated ducts in the board supported configuration. Jaiman et al. [11] presented a numerical study to investigate the pressure drop reduction potential of liners in a corrugated pipe. The results provided a consistent estimate of the pressure drop and friction factor for varying flow rates, and also revealed complex internal turbulent structures within the duct. Afterward, Weaver [12] conducted a comprehensive experimental research on pressure loss for airflow in corrugated ductwork. Their results extended the existing ASHRAE/ACCA data for a corrugated duct, and also demonstrated that some configurations could exhibit over ten times the pressure loss found in a rigid duct or fully stretched corrugated duct of the same diameter. Cantrill [2] further investigated the pressure drop in corrugated ducts with relatively larger diameters (i.e., 12, 14, 16 in.). The results showed that pressure losses for compression ratios greater than 4% could be over four times greater than for maximally stretched corrugated ducts. Their findings were supposed to be added to the existing ASHRAE and industry data for corrugated duct.

On the other hand, corrugated ducts can be generally forced to make bends due to installation restrictions, which is expected to induce excess pressure loss owing to the striking turbulent flow behavior within the bent duct [13, 14]. Although a great number of researches have been carried out on flow behavior in smooth ducts with a 90° bend [15–17], rare work has been reported on flow field as well as pressure loss of a bent corrugated duct. Kulkarni and Idem [18] conducted an experimental study on pressure loss coefficient of bends in fully stretched nonmetallic corrugated ducts. They found that the bend radius had a significant effect on the loss coefficient. In addition, the pressure loss under a larger bend angle condition could be primarily controlled by dynamic effects due to flow separation, swirl, and turbulence generation in the curved region. It should be noted that even in a straight pipe, the swirled turbulent flow could have apparent effects on particle and droplet deposition [19].

Even though a certain number of researches [10, 11, 20] have been performed on pressure loss of straight run corrugated ducts, to the authors' best knowledge, there is a lack of information concerning the pressure drop and turbulent flow behavior in bent corrugated ducts with various bend angles. Since the duct bend is supposed to induce the typical flow separation and a pair of cross-sectional vortices (i.e., the Dean vortices) [16, 21], it is of significant importance to study the effect of bend angle on pressure drop and flow behavior in corrugated ducts.

In this study, the effect of bend angle on pressure drop and flow behavior within a relatively small-diameter (i.e., 1 in.) corrugated duct is numerically investigated and experimentally validated under a fully developed flow condition. The large eddy simulation (LES), together with the proper orthogonal decomposition (POD) method, is employed to study the pressure drop, mean flow pattern and unsteady flow evolution for a corrugated duct with various bend angles (i.e.,  $\beta = 0^\circ, 30^\circ, 60^\circ, 90^\circ$ ). For the experimental validation, an open-circuit low-speed wind tunnel is designed and fabricated to test the typical pressure drop of a corrugated duct with varying bend angles. The present study aims to illustrate the fundamental flow behavior as well as the corresponding pressure loss pertinent to the airflow passing through the corrugated duct with various bend angles.

## 2 Numerical method

Although steady numerical simulation can usually be expected to solve some integrated values (e.g., pressure drop, drag coefficient, etc.) [22, 23], it always fails to reveal the realistic unsteady flow behavior since the flow field is generally computed based on the Reynolds-averaged Navier–Stokes (RANS) equations [24]. Hence, in order to get a better insight into the flow behavior in the corrugated duct with different bend angles, the large eddy simulation (LES) is performed to investigate the effect of bend angle on pressure drop and flow behavior in the corrugated duct.

### 2.1 Subgrid-scale model

In the present study, the large eddy simulations are performed by solving the standard form of the filtered Navier–Stokes (Eq. (1)) and continuity (Eq. (2)) equations for incompressible fluid, closed with the dynamic Smagorinsky-Lilly subgrid-scale (SGS) model [25–27]:

$$\frac{\partial \bar{u}_i}{\partial t} + \frac{\partial \bar{u}_i \partial \bar{u}_j}{\partial x_j} = -\frac{\partial \bar{P}}{\partial x_i} + \frac{\partial (2\nu \bar{S}_{ij})}{\partial x_j} - \frac{\partial \tau_{ij}}{\partial x_j}, \tag{1}$$

$$\frac{\partial \bar{u}_i}{\partial x_i} = 0. \tag{2}$$

Here,  $\bar{S}_{ij} = 0.5 (\partial \bar{u}_i / \partial x_j + \partial \bar{u}_j / \partial x_i)$  is the filtered rate of strain tensor, and  $\nu$  is the kinetic dynamic viscosity.  $\tau_{ij} = \bar{u}_i \bar{u}_j - \bar{u}_i \bar{u}_j$  (i.e., the subgrid-scale stress) represents the stresses due to subgrid-scale motions, which can be modeled using the Boussinesq approximation [28]

$$\tau_{ij} = \frac{1}{3} \delta_{ij} \tau_{kk} - 2\mu_t \bar{S}_{ij}, \tag{3}$$

where  $\delta_{ij}$  is the Kronecker delta;  $\tau_{kk}$  is the isotropic part of the subgrid-scale stresses which is not modeled, but added to the filtered static pressure term;  $\mu_t$  is the subgrid-scale eddy viscosity, which is evaluated by the dynamic Smagorinsky–Lilly model [25–27]

$$\mu_t = C_D \Delta^2 \sqrt{2\bar{S}_{ij}\bar{S}_{ij}}, \tag{4}$$

where  $\Delta$  is the filter width (computed as the cube root of the cell volume) and  $C_D$  is calculated using the dynamic method proposed by Lilly [27]. To avoid numerical instability, the cell-centered values of the coefficient  $C_D$  are evaluated as the local average of face values and the effective viscosity is also clipped to zero by default.

### 2.2 Computational domain

Since corrugated ducts generally have higher resistance to air flow, slightly larger ducts are generally required to carry the same volume of air as compared to smooth ducts [29]. In this context, a relatively small-diameter (i.e.,  $D = 1$  in.) corrugated duct, which is rarely studied before and featured with higher pressure loss, is employed as the research object for this work. Figure 1a shows the schematic of computational domain and the detailed

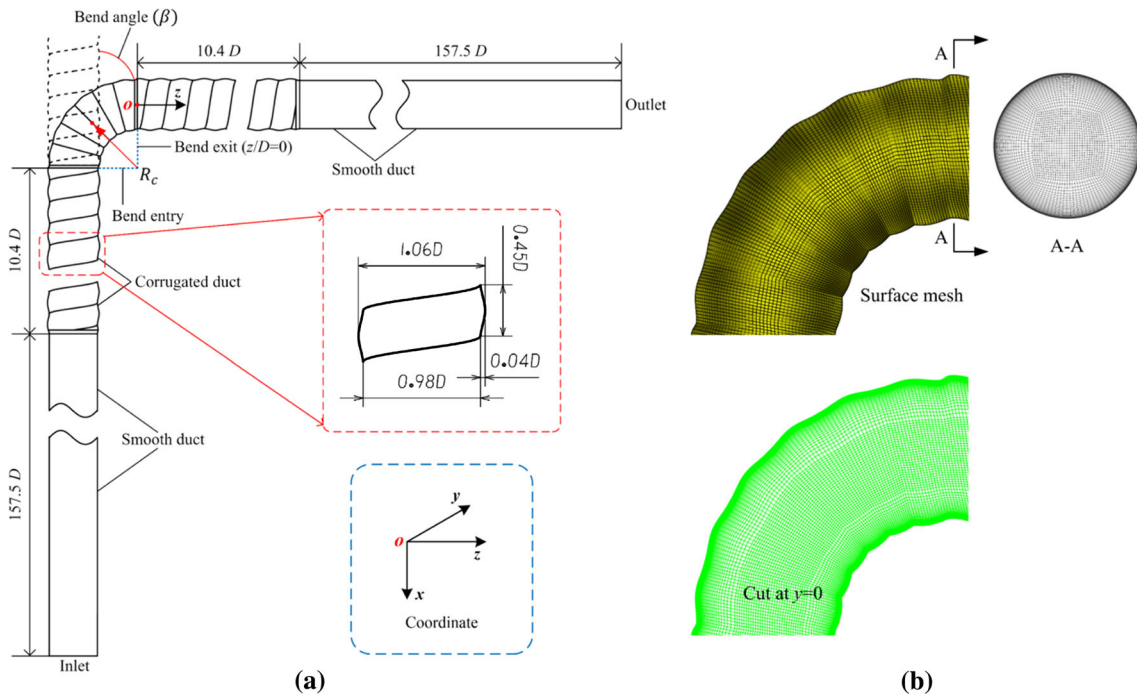


**Fig. 1** **a** Schematic of computational domain and geometric parameters of the corrugated duct; **b** grid distribution within the bend region

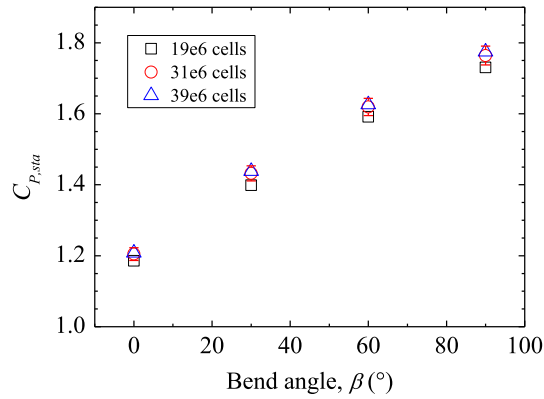


**Fig. 2** Grid independence study—pressure drop ( $C_{P,sta}$ ) varies with the bend angle and the number of cells

geometric parameters of the corrugated duct. Two smooth ducts both with a length of  $157.5 D$  are mounted at the upstream and downstream of the corrugated duct, respectively. This is aimed to ensure a full development before the air enters into the corrugated duct, as well as to mimic the general engineering scenarios where a corrugated duct is applied. The air entering the upstream smooth duct is modeled with the Mass-Flow Inlet Boundary Condition (i.e.,  $\dot{m} = \rho u_n A = 7.97 \times 10^{-3} \text{ kg/s}$ ), which is designed to make the Reynolds number ( $Re$ ) close to  $2.2 \times 10^4$ . The air leaving the downstream smooth duct is modeled by the pressure outlet boundary condition, which defines the local static pressure as the standard atmospheric pressure (i.e.,  $P_{sta} = 101325 \text{ Pa}$ ). Both the smooth and corrugated ducts are modeled as no-slip walls (i.e.,  $\partial P / \partial n, U = 0$ ). In order to study the effect of bend angle on pressure drop and flow behavior in the corrugated duct, a corrugated duct with various bend angles (i.e.,  $\beta = 0^\circ, 30^\circ, 60^\circ$  and  $90^\circ$ ) but with the same length ( $L = 550 \text{ mm}$ ), effective diameter ( $D = 1 \text{ in.}$ ) and bend curvature ratio ( $\gamma = R/R_c = 0.46$ , where  $R$  is the effective radius of corrugated duct and  $R_c$  the bend centerline radius) is designed and explored. Figure 1a represents the case for  $\beta = 90^\circ$ , and the origin of coordinates is located at the center of the bend exit (i.e.,  $z/D = 0$ ). In this study, the high-quality hexahedral mesh is generated within the computational domain. In order to achieve an accurate prediction of the flow behavior near the duct wall, the first hexahedral layer is constructed at a distance of  $0.02 \text{ mm}$  together with a 10% increase in grid size from the wall, which renders the wall  $y^+$  to be less than 1 (Fig. 1b). The corrugated duct part, i.e., the region of interest, is set as the grid refinement region (Fig. 1b), which generally consists of denser hexahedral meshes. Then, a grid independence study is performed on three different sets of grids as shown in Fig. 2. It can be found that the pressure drop ( $C_{P,sta}$ ) defined by Eq. (5) exhibits a minor variation as the cell increases from 31e6 to 39e6. Specifically, the results of 39e6 cells is found to be located within the 1.5% error bar of the results of 31e6 cells. Hence, the grid pattern consisting of 31 million cells can be expected to give a reasonable prediction with respect to the pressure loss and flow behavior for each corrugated duct case.

### 2.3 Numerical solution methodology

In this work, the finite volume method is used to solve the three-dimensional filtered Navier–Stokes equations on unstructured meshes, using the cell-centered collocated variable arrangement. The second-order accurate upwind-biased scheme QUICK [30,31] is used to discretize diffusive and convective terms in the momentum equations. Time marching is performed by using a second-order implicit scheme. The iterative pressure correction algorithm SIMPLE is used for the coupling of velocity and pressure. In order to keep a stable convergence behavior during the computation, the under-relaxation factors for both pressure and momentum are set to 0.3. The time step  $\Delta t$  is set to  $4 \times 10^{-5} \text{ s}$  and is kept constant during the simulation, which maintains the value of the Courant–Friedrichs–Lewy (CFL) number at less than 1. At each time step, 15 iterations are employed to ensure the normalized residuals of equations to fall below the value of  $10^{-5}$ . The collection of results for the turbulence statistics starts after a certain time of  $20t^*$  ( $t^* = L/W_b$ , where  $W_b$  is the inlet velocity), and then continues over a period of about  $30t^*$ .



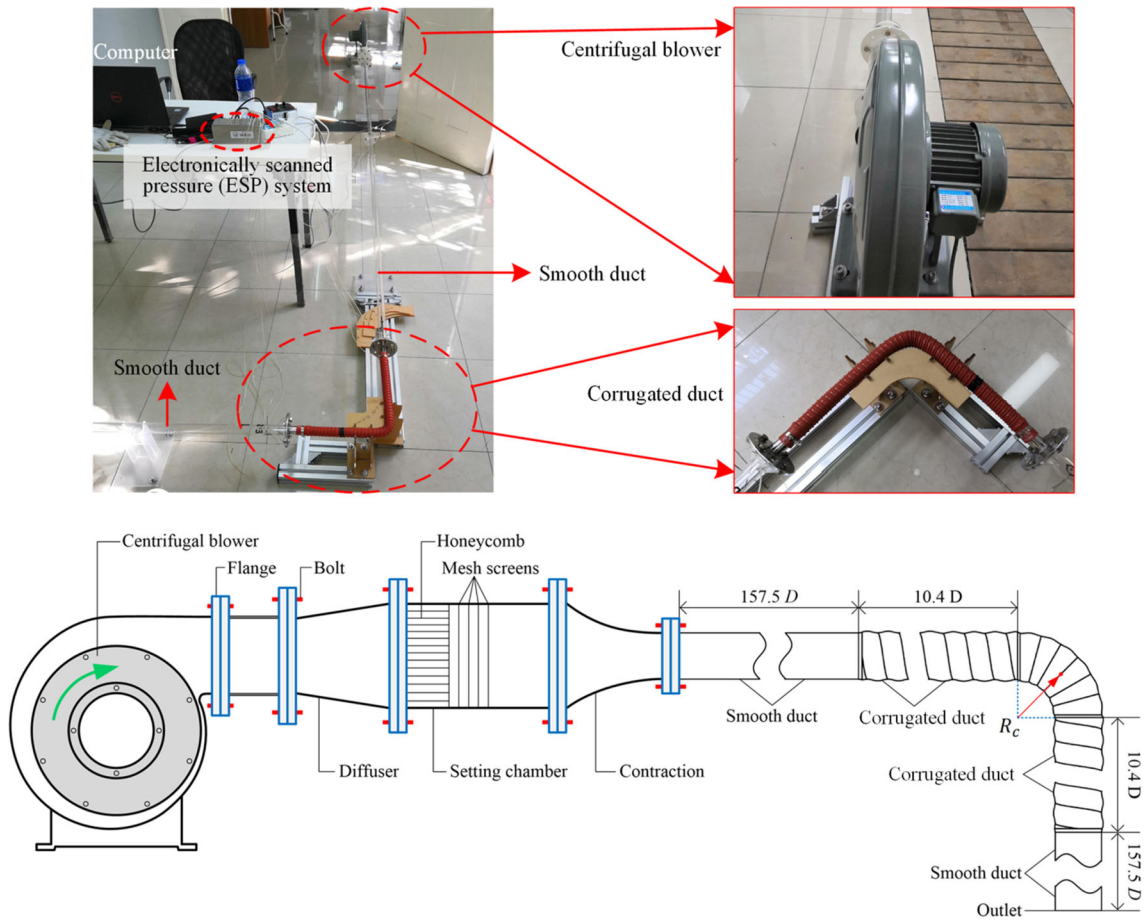


Fig. 3 Experimental setup for pressure drop measurement of the corrugated duct

### 3 Experimental

Figure 3 shows the schematic of the experimental setup for pressure drop measurement of the corrugated duct, which is mainly aimed at validating the numerical simulations. An open-circuit low-speed wind tunnel, consisting of a high-power centrifugal blower (Yong Cheng CZ-TD370W220v), a diffuser, a setting chamber and a contraction, is designed and fabricated with considerable care to generate nearly identical flow conditions to that of simulations. The tested duct assembly, as described in Sect. 2.2 (i.e., Fig. 1a), is directly connected to the contraction. The wind speed is measured by a hot-wire anemometer (TSI 9535,  $\pm 0.015$  m/s). With the application of pressure tubes and electronically scanned pressure (ESP) system (Scanivalve Corp DSA3217,  $\pm 0.02\%$  FS), the pressure drop of the corrugated duct can be finally obtained, which is expressed in a nondimensional form

$$C_{P,sta} = \frac{\Delta P}{0.5\rho W_b^2}, \quad (5)$$

where  $\Delta P$  represents the pressure drop of the corrugated duct,  $\rho$  represents the density of the air. Since it is difficult to drill mini holes for pressure measurements on the present corrugated duct, two pressure taps are set up on the smooth ducts, which lie at about  $2.17D$  upstream and  $2.56D$  downstream the corrugated duct, respectively. The uncertainty analysis of the experimental test is carried out according to the methodology proposed by Mof-fat [32] based on Eq. (5). It is found that in the worst-case scenario, the measurement error is less than 0.27%, which is taken as the cut-off value to judge the reliability of an experiment when performing the repetitive tests.

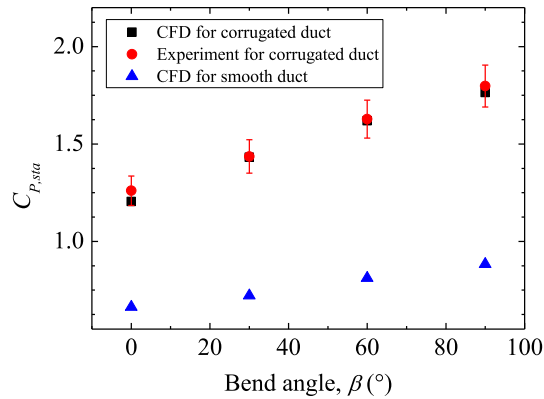


**Fig. 4** Comparison of pressure drops between numerical simulations and experimental tests under various bend angles, and numerical results of pressure drops for smooth duct with the same bend angle of the corrugated duct

## 4 Results and discussion

### 4.1 Validation of the numerical simulations

Figure 4 shows the comparison of pressure drops of the corrugated duct under various bend angles between numerical simulations and experiments. As can be seen, each simulation result is found to be located within the 6% error bar of the experimental data. This indicates that the pressure drop of the corrugated duct can be accurately predicted by the present numerical model. Meanwhile, the pressure drop exhibits an apparent increase trend with the increase of the bend angle. Specifically, as the bend angle increases from  $0^{\circ}$  to  $90^{\circ}$ , the pressure drop is found to increase by about 43%. This implies that an increase in bend angle can be expected to induce a larger pressure loss, thus rendering severer energy loss. On the other hand, in comparison with the corrugated duct, the smooth duct with the same bend angle of the corrugated duct shows a much smaller pressure drop (e.g., nearly half of the corrugated duct). This implies that the intrinsic roughness nature of the present corrugated wall is supposed to play a significant role in causing the higher pressure drop. In addition, as for the distribution pattern of the pressure drop, it can be found that the pressure drop of the corrugated duct seems to be more sensitive to the bend angle. In the next sections, we will mainly focus on revealing the effect of bend angle on pressure drop and flow behavior in the corrugated duct.

### 4.2 Mean flow field

Figure 5 shows the contour maps of the time-averaged streamwise velocity scaled by the inlet velocity ( $W_b$ ) for the four downstream stations (i.e.,  $z/D = 0, 2, 4, 6$ ) and for the four bend angles (i.e.,  $\beta = 0^{\circ}, 30^{\circ}, 60^{\circ}, 90^{\circ}$ ). This figure is mainly aimed to demonstrate the effect of centrifugal force on the duct flow for streamwise velocity component. It is observed that in cases of the bent corrugated duct (i.e.,  $\beta = 30^{\circ}, 60^{\circ}, 90^{\circ}$ ), the high-velocity fluid is pushed toward the outer wall of the duct, while the low-velocity one is deflected toward the inner wall, thus forming a C-shaped velocity distribution. However, in case of the straight corrugated duct (i.e.,  $\beta = 0^{\circ}$ ), a quasi-symmetric velocity distribution is found to emerge in cross sections. Moreover, with an increase in the bend angle, the C-shaped velocity pattern appears to be more striking, and then it tends to decay more rapidly as the flow moves further downstream. Such a phenomenon can be explained by the fact that the milder the bend angle, the weaker the centrifugal force, therefore the smaller the velocity gradient created along the duct cross section.

Figure 6 shows mean in-plane streamlines superimposed with mean streamwise vorticity ( $\omega_z$ ) contours for the four downstream stations and for the four bend angles. This figure mainly deals with the secondary flow induced by the bend angle and primarily depicts the flow patterns for crosswise velocity component. As reported in massive previous work focusing on smooth bent duct/pipe [16], the development of the Dean cells is also clearly revealed in the present bent-corrugated duct. Meanwhile, some important information can be obtained from those time-averaged Dean cells. Firstly, the cell center tends to move toward the center of the corrugated duct as the flow travels further downstream for each bent duct case, which is found to be accompanied by the relaxing of the airflow and damping of the bend angle effect (Fig. 5). Secondly, an increase in



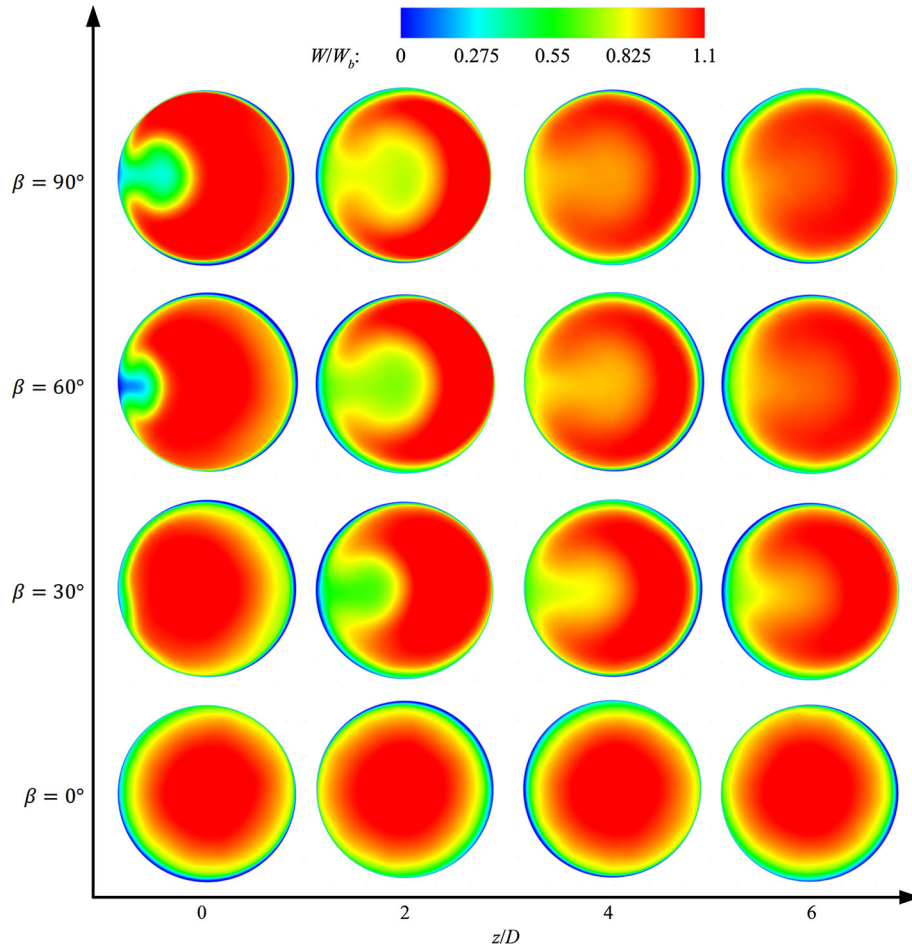


**Fig. 5** Mean streamwise velocity distributions in cross sections (plane at  $z/D = 0, 2, 4, 6$ ) downstream the bend under various bend angles ( $\beta = 0^\circ, 30^\circ, 60^\circ, 90^\circ$ )

bend angle appears to induce a higher vorticity level within the Dean cells region, which is expected to cause a larger pressure loss for the duct flow.

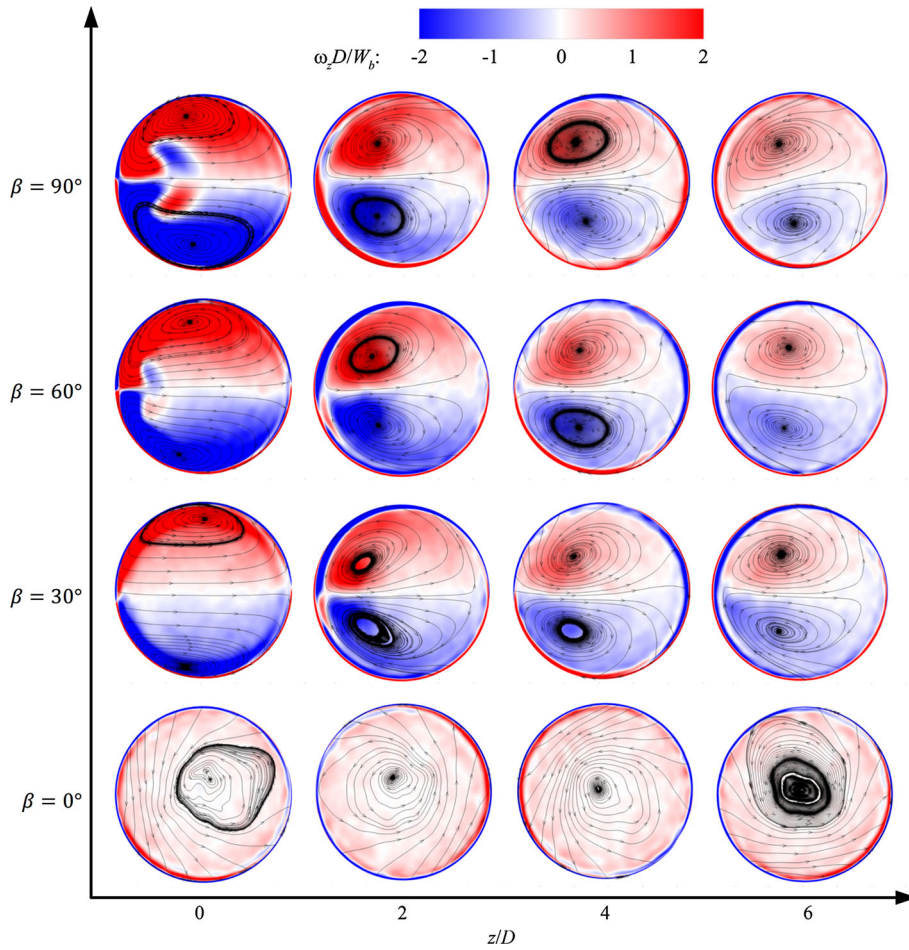
In order to quantitatively study the effect of bend angle on the swirl intensity distribution within the corrugated duct, the swirl number defined by Gupta et al. [33] is introduced as

$$Sw = \frac{\int_{r < R} r U_\theta U_{ax} dA}{R \int_{r < R} |U_{ax}| U_{ax} dA}, \tag{6}$$

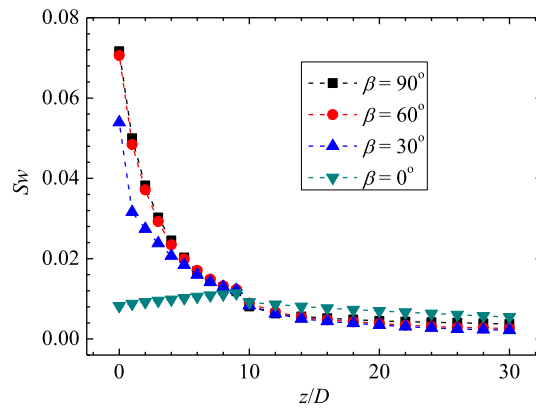
where  $U_\theta$  and  $U_{ax}$  are the tangential and axial velocity components. In this context, the swirl number can be regarded as the ratio between the flux of angular momentum in the axial direction and the flux of axial momentum in the axial direction, which is normalized with the duct radius. The swirl number (Sw) distribution can be achieved based on sample planes downstream the bend as shown in Fig. 7. It is observed that the swirl intensity appears to experience a quasi-exponential decay along the bent corrugated duct. Meanwhile, an increase in the bend angle tends to induce a larger swirl intensity distribution especially near the bend exit region (e.g.,  $z/D < 10$ ). These quantitative results are found to be well-consistent with the qualitative findings (Fig. 6).

Figure 8 shows the time-averaged distributions of the total pressure loss coefficient in longitudinal sections (i.e., at  $y/D = 0$ ) within the corrugated duct under four bend angles (i.e.,  $\beta = 0^\circ, 30^\circ, 60^\circ, 90^\circ$ ). Here, the total pressure loss coefficient ( $C_{P,tot}$ ) is defined by

$$C_{P,tot} = \frac{P_{t0} - P_t}{0.5 \rho W_b^2}, \tag{7}$$



**Fig. 6** Mean in-plane streamlines superimposed with mean streamwise vorticity contours in cross sections (plane at  $z/D=0, 2, 4, 6$ ) downstream the bend under various bend angles ( $\beta = 0^\circ, 30^\circ, 60^\circ, 90^\circ$ )



**Fig. 7** Swirl number distributions downstream the bend under various bend angles

where  $P_{10}$  is the total pressure at the inlet,  $P_l$  is the local total pressure within the corrugated duct. As can be seen, a striking pressure loss pattern appears to emerge toward the inner wall at the onset of the bend (Figs. 8a–c). This is due to the centrifugal force caused by the bend which induces a typical flow separation near the inner wall of the bend. On the contrary, as for the straight corrugated duct, the flow experiences a mild pressure loss with the growth of the boundary layer. Additionally, an increase in bend angle is found to produce higher pressure loss as well as a larger pressure loss area near the inner wall of the bend, which

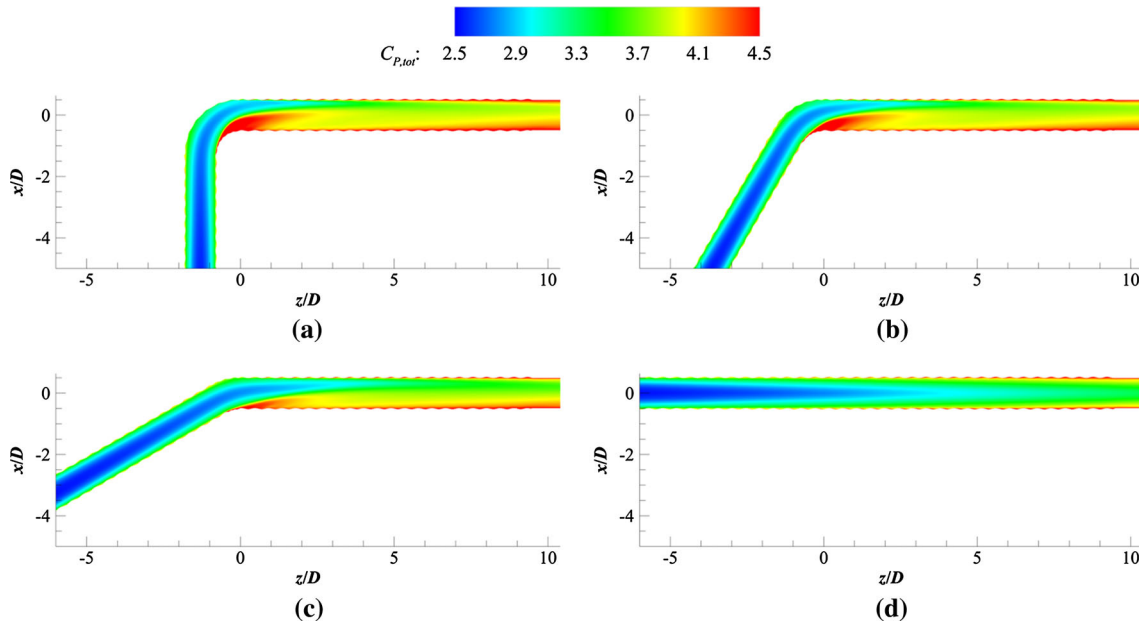


**Fig. 8** Time-averaged total pressure loss coefficient distributions in longitudinal sections (plane at  $y/D = 0$ ) within the corrugated duct under various bend angles

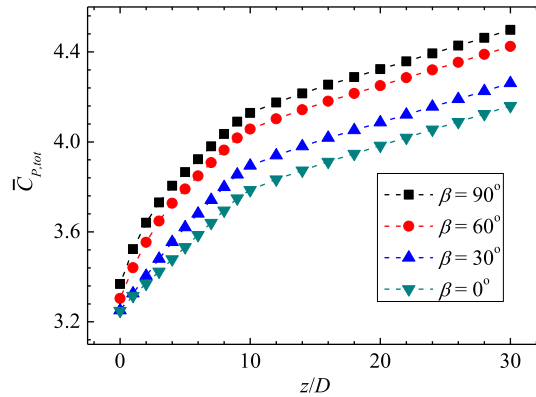


**Fig. 9** Evolution of mass averaged total pressure loss coefficient downstream the bend under various bend angles

appears to be well-consistent with distributions of the mean streamwise vorticity (Fig. 6). This is believed to further widen the high pressure loss region downstream the bend.

In order to further compare the total pressure loss reduction performance of the corrugated duct quantitatively, the overall mass averaged total pressure loss coefficient ( $\bar{C}_{P,tot}$ ) defined by Eq. (8) is calculated and presented in Fig. 9,

$$\bar{C}_{P,tot} = \frac{\sum_i \sum_j (\rho u_n C_{P,tot} dA)_{ij}}{\sum_i \sum_j (\rho u_n dA)_{ij}}, \tag{8}$$

where  $u_n$  is the normal velocity to the measurement plane. For the corrugated duct,  $\bar{C}_{P,tot}$  exhibits a monotonic increase along the duct downstream the bend. As it is anticipated, the largest bend angle (i.e.,  $\beta = 90^\circ$ ) is found to induce the steepest increase in  $\bar{C}_{P,tot}$ , thus rendering the severest pressure drop downstream the bend (Fig. 4). Specifically,  $\bar{C}_{P,tot}$  appears to experience a remarkable increase as  $\beta$  increases from  $30^\circ$  to  $60^\circ$ . Conversely,  $\bar{C}_{P,tot}$  tends to exhibit a relatively mild increase when  $\beta$  increases from  $60^\circ$  to  $90^\circ$ .

4.3 Unsteady flow behavior

4.3.1 Instantaneous flow field

In order to capture the dynamic behavior of airflow passing through the bent corrugated duct, this section mainly discusses the unsteady flow features within the duct. Figure 10 shows the instantaneous velocity distributions in longitudinal and cross sections with various bend angles. As can be seen, the high mass and momentum transfer are generated by the secondary motion induced by the centrifugal force acting on the fluid in the bent sections. This secondary motion takes the shape of two counter-rotating vortices (i.e., the Dean vortices), which moves

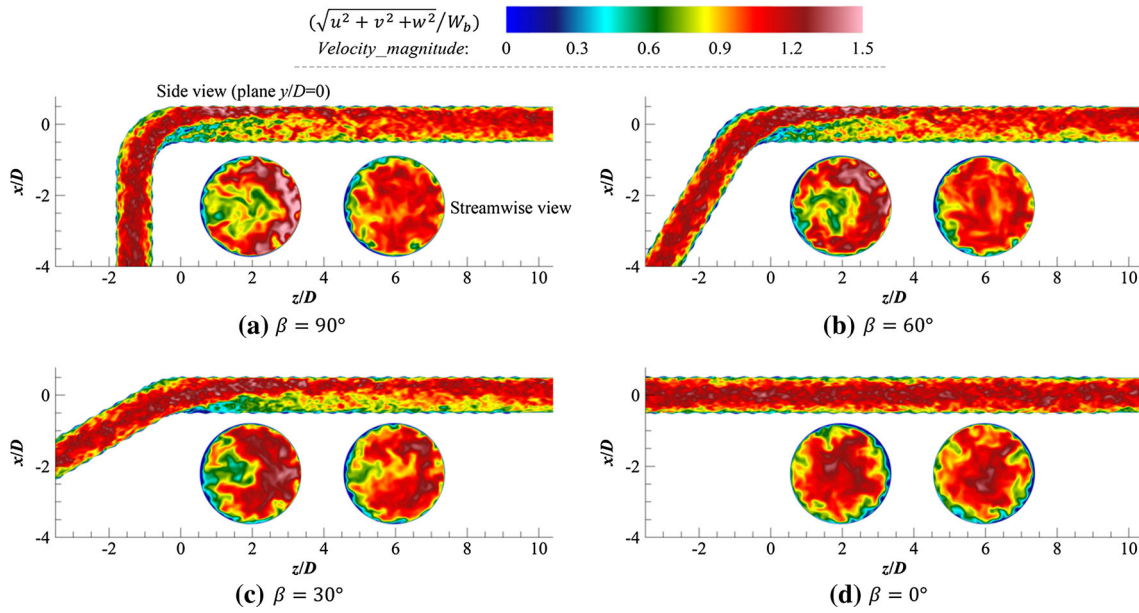


Fig. 10 Instantaneous velocity distributions in longitudinal (plane at  $y/D = 0$ ) and cross (plane at  $z/D = 2, 6$ ) sections with various bend angles

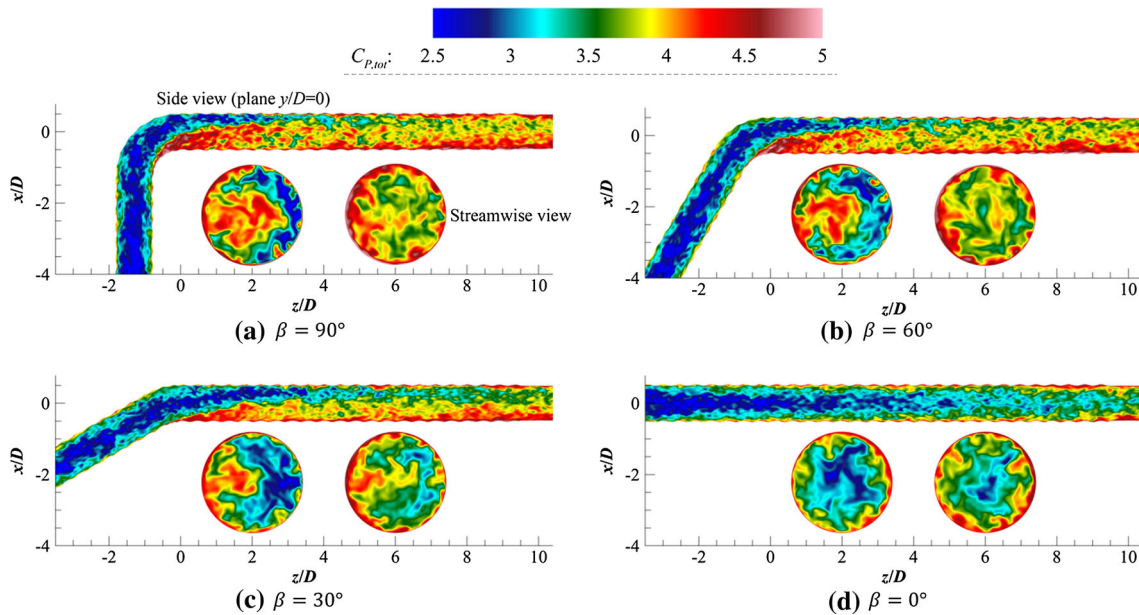


Fig. 11 Instantaneous total pressure loss coefficient distributions in longitudinal (plane at  $y/D = 0$ ) and cross (plane at  $z/D = 2, 6$ ) sections with various bend angles

the fluid toward the outside of the bend and back toward the inside along the wall, thus increasing the mass and momentum transfer across the duct section. The Supplementary Movie 1 further depicts the detailed unsteady behavior of the Dean vortices as well as the effect of bend angle on flow separation. It can be observed that the larger bend angle appears to induce stronger centrifugal force, therefore causing larger-scale flow separation and more intense Dean vortices near the bend (e.g., at  $z/D = 2$ ). Accordingly, a more striking pressure loss pattern originating from the inner wall of the bend is found to emerge (Fig. 11 and Supplementary Movie 2), which renders a substantial pressure drop in the corrugated duct as quantitatively shown in time-averaged results (Fig. 9).

4.3.2 POD analysis

In order to get a better insight into the flow structure evolution in the corrugated duct, the snapshot proper orthogonal decomposition (POD) method [34] is employed to define and extract dominant flow structures from turbulent flow field, which is based on the proper orthogonal theorem of probability [35] as proposed by Lumley [36]. Readers may refer to Sirovich [34] and Taira et al. [37] for the details of the snapshot POD method, which is believed to be one of the most efficient way to extract the most energetic components of an infinite dimensional process with only a few modes [38]. When applied to results of unsteady numerical simulation, the POD could be viewed as a filtering device used to objectively eliminate the low-energy motions of the flow that would obscure the main energetic features of the flow [24,39]. Briefly, the first step for the snapshot POD implementation is to calculate the mean velocity field  $\bar{u}(\xi)$ , which is then removed from each of instantaneous snapshots  $u(\xi, t)$ . The rest of analysis works on the fluctuating components of the velocity

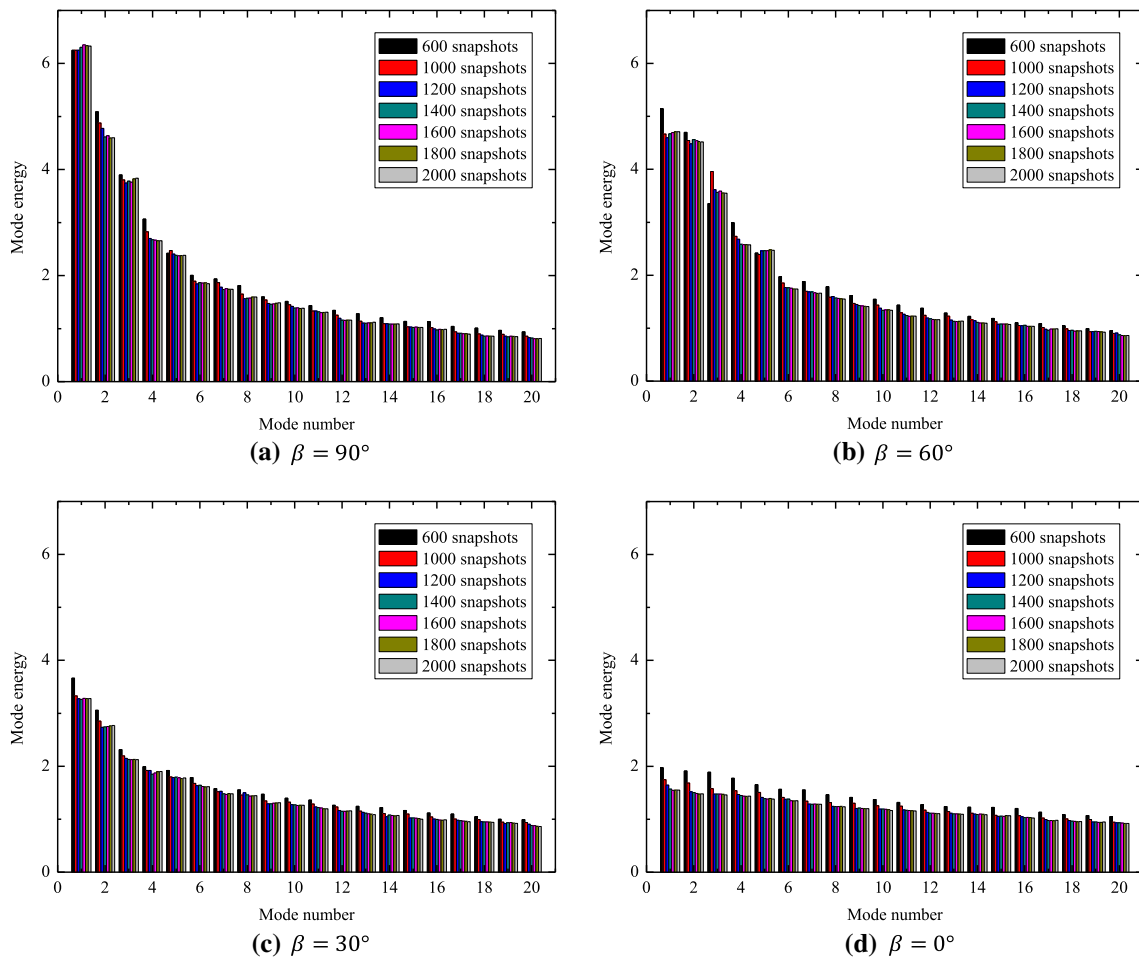


Fig. 12 POD mode energy (TKE) distribution with various numbers of snapshots and bend angles in the cross section of  $z/D = 2$ : a  $\beta = 90^\circ$ ; b  $\beta = 60^\circ$ ; c  $\beta = 30^\circ$ ; d  $\beta = 0^\circ$



$u(t)$ . Given the flow field  $u(\xi, t)$ , snapshots of the flow field are stacked in a collection of column vectors:

$$u(t) = u(\xi, t) - \bar{u}(\xi) \in \mathbb{R}^n, t = t_1, t_2, \dots, t_m, \tag{9}$$

where  $u(t)$  represents the fluctuating velocity component with the time-averaged value  $\bar{u}(\xi)$  removed of the original velocity vector  $u(\xi, t)$ . Generally, the objective of the POD analysis is to find the optimal basis vectors that can best represent the given data. Hence, the solution to this problem [40] can be determined by finding the eigenvectors  $\psi_j$  and the eigenvalues  $\lambda_j$  from

$$\mathbf{R}\psi_j = \lambda_j\psi_j, \psi_j \in \mathbb{R}^m, \lambda_1 \geq \lambda_2 \geq \dots \geq \lambda_m \geq 0, m \leq n, \tag{10}$$

where  $\mathbf{R}$  is the covariance matrix of the vector  $u(t)$ . Hence,  $\mathbf{R}$  can be expressed as

$$\mathbf{R} = \sum_{i=1}^m u^T(t_i) u(t_i) = \mathbf{U}^T \mathbf{U} \in \mathbb{R}^{m \times m}, \tag{11}$$

where the matrix  $\mathbf{U}$  represents the  $m$  snapshot data stacked into a matrix form of

$$\mathbf{U} = [u(t_1) u(t_2) \dots u(t_m)] \in \mathbb{R}^{n \times m}. \tag{12}$$

The size of the covariance matrix  $n$  is based on the spatial degrees of freedom of the data. For flow field data,  $n$  is generally large and equal to a value resulting from the number of grid points timing the number

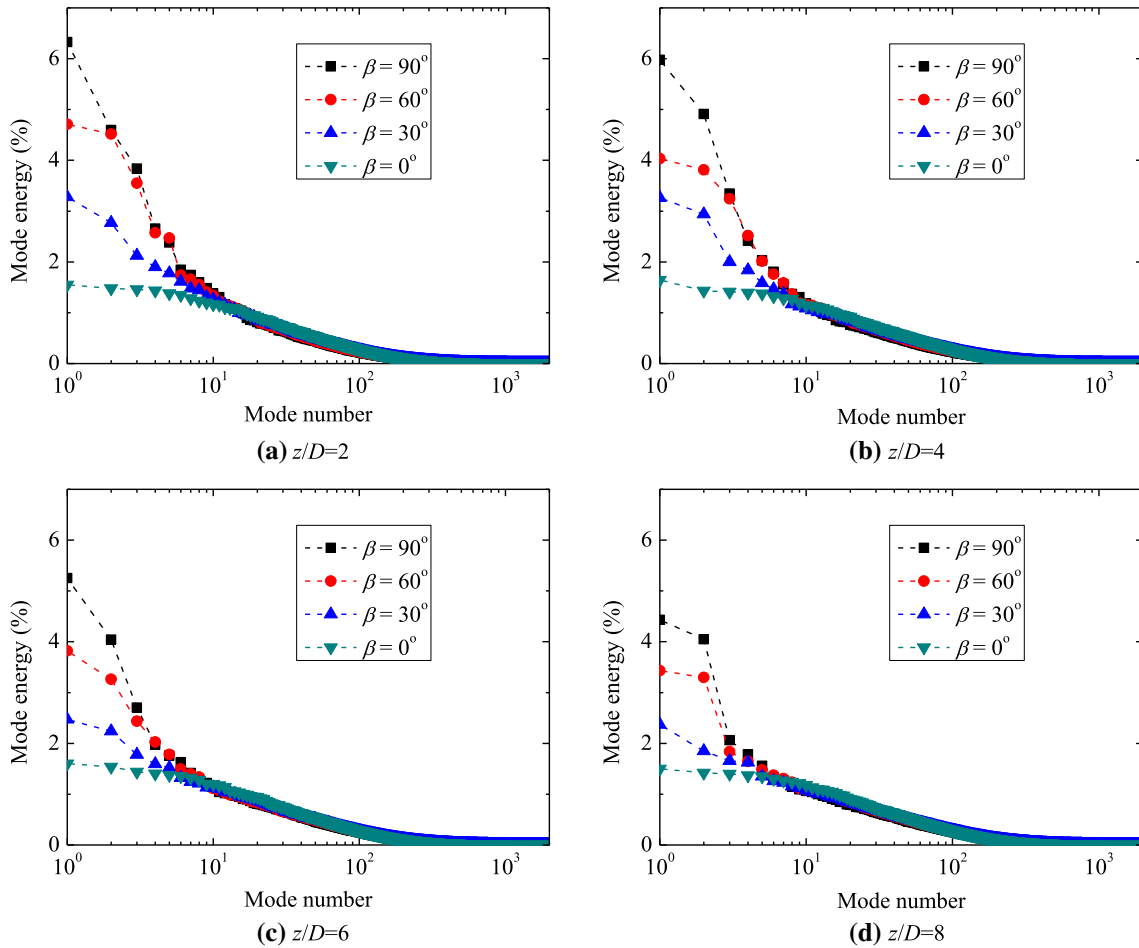


**Fig. 13** Scaled mode energy of the fluctuating energy in cross sections with various bend angles: **a**  $z/D = 2$ ; **b**  $z/D = 4$ ; **c**  $z/D = 6$ ; **d**  $z/D = 8$



of variables considered during the POD analysis. With the eigenvectors  $\psi_j$  of the above smaller eigenvalue problem determined, the POD modes ( $\phi_j$ ) can be retrieved through

$$\phi_j = U\psi_j \frac{1}{\sqrt{\lambda_j}} \in \mathbb{R}^n, \quad j = 1, 2, \dots, m. \tag{13}$$

Here, during the vector operation, the POD modes can also be expressed in a matrix form

$$\Phi = U\Psi \Lambda^{-1/2}, \tag{14}$$

where  $\Phi = [\phi_1 \phi_2 \dots \phi_m] \in \mathbb{R}^{n \times m}$ ,  $\Psi = [\Psi_1 \Psi_2 \dots \Psi_m] \in \mathbb{R}^{m \times m}$ ,  $\Lambda = [\lambda_1; \lambda_2; \dots; \lambda_m] \in \mathbb{R}^m$ . When the fluctuating velocity component  $u(t)$  is handled during the POD analysis, the eigenvalues  $\lambda_j$  represent the turbulent kinetic energy (TKE) captured by each mode. Hence, these eigenvalues can be employed to determine the number of POD modes required to represent the major turbulent fluctuations for the flow field. Generally, during the POD analysis, the first  $N$  POD modes are retained to express the flow field which can be defined as

$$\sum_{i=1}^N \lambda_j / \sum_{i=1}^n \lambda_j \approx 1. \tag{15}$$

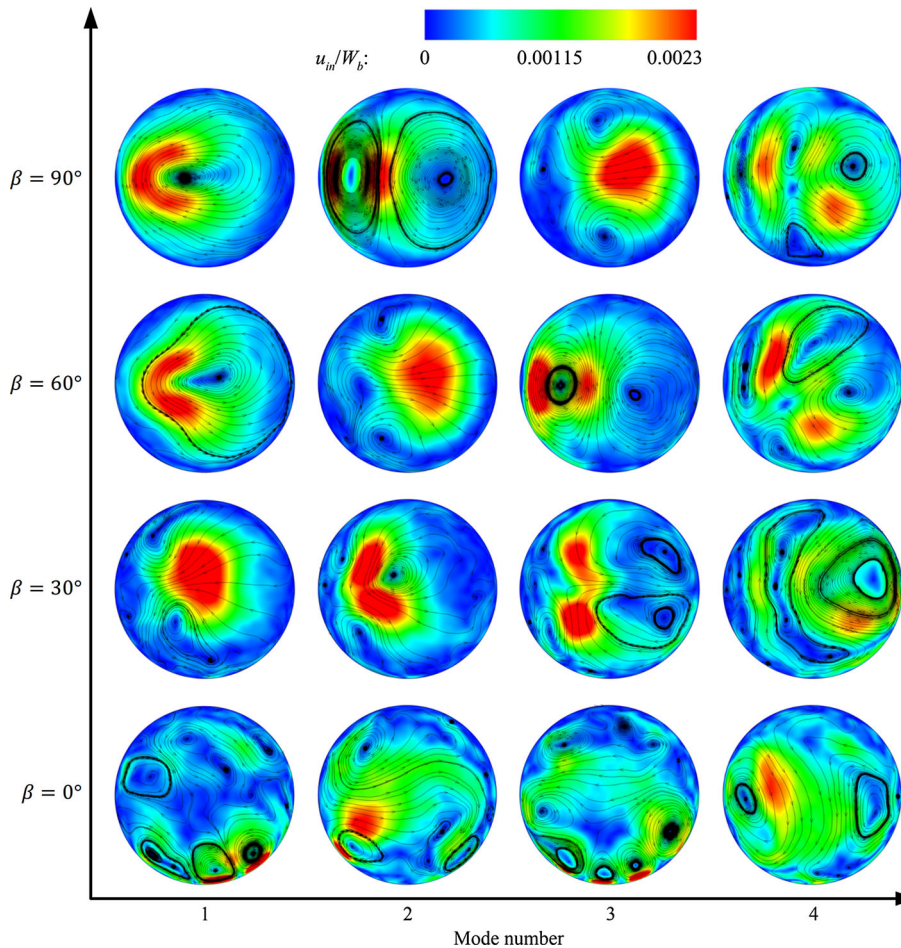


**Fig. 14** The first four POD modes plotted as sectional streamlines and in-plane velocity contours for the corrugated duct at the downstream station  $z/D = 2$  under various bend angles

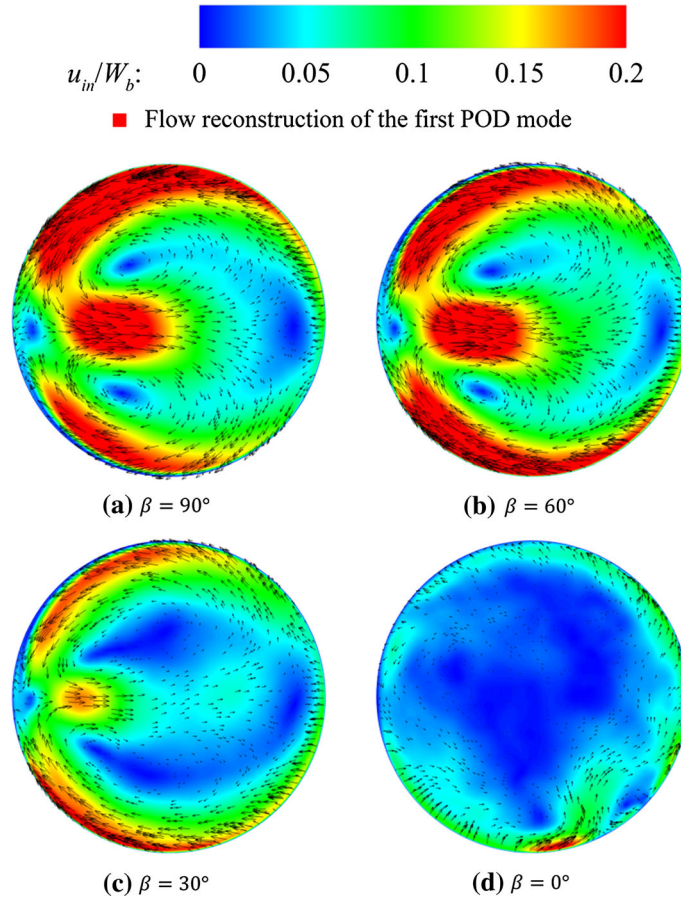
With the important POD modes determined, the flow field is expected to be characterized by a finite or truncated series

$$u(\xi, t) \approx \bar{u}(\xi) + \sum_{j=1}^N a_j(t)\phi_j(\xi), \tag{16}$$

$$a_j(t) = \langle u(\xi, t) - \bar{u}(\xi), \phi_j(\xi) \rangle = \langle u(t), \phi_j(\xi) \rangle, \tag{17}$$

where  $a_j(t)$  are the temporal coefficients corresponding to each POD mode. In this context, the high-dimensional ( $n$ ) flow field is expected to be effectively reduced to an optimal one, i.e., a representation only with the first  $N$  modes.

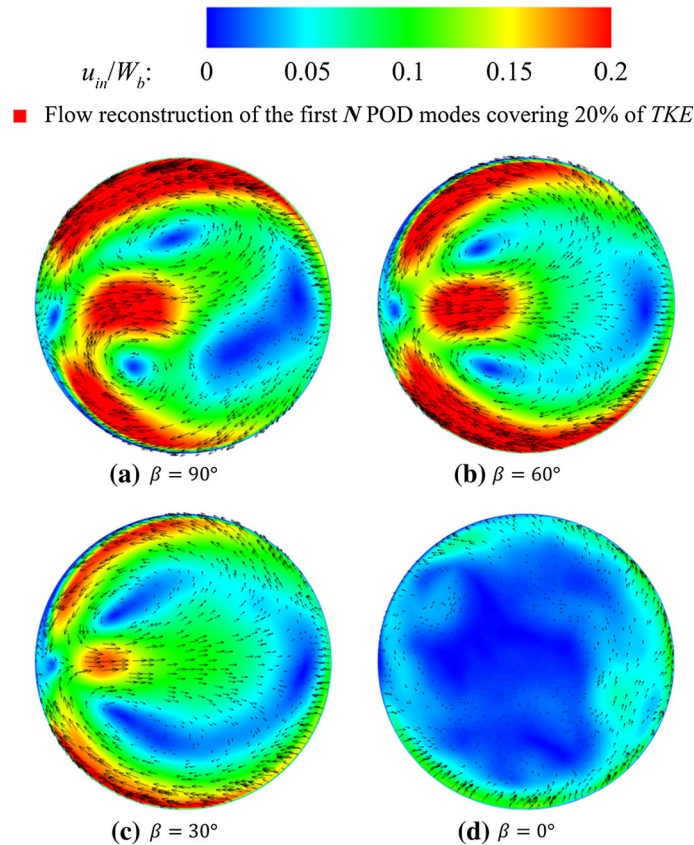
Figure 12 shows the effect of the number of snapshots on the POD mode with respect to the mode energy (i.e., TKE) distributions for the first twenty modes in the cross section of  $z/D = 2$  with various bend angles. As can be seen, the mode energy is found to be nearly convergent when the number of snapshots exceeds a value of 1500. Hence, it is supposed to be reasonable to employ 2000 snapshots to extract the spatial modes in cross sections for this work. Figure 13 shows the scaled mode energy of the fluctuating energy in cross sections (i.e., plane at  $z/D = 2, 4, 6, 8$ ) with various bend angles. As apparent, with the increase in the bend angle, the first few (e.g., four) modes start to account for larger portion of fluctuating energy for all cross sections. This implies that a larger bend angle is expected to promote the inheritance of turbulent energy for the first most energetic modes, thus enhancing the potential strength of the Dean cells. In addition, for the bent corrugated duct (i.e.,  $\beta = 30^\circ, 60^\circ, 90^\circ$ ), the mode energy is found to experience a striking decline as the flow moves downstream. This means that the Dean cells tend to undergo a general decay due to the weakening effect of the centrifugal force, which is well-consistent with the finds of the time-averaged results (Fig. 6).



**Fig. 15** The flow reconstruction of the first POD mode in cross sections at  $z/D = 2$  under various bend angles: **a**  $\beta = 90^\circ$ ; **b**  $\beta = 60^\circ$ ; **c**  $\beta = 30^\circ$ ; **d**  $\beta = 0^\circ$

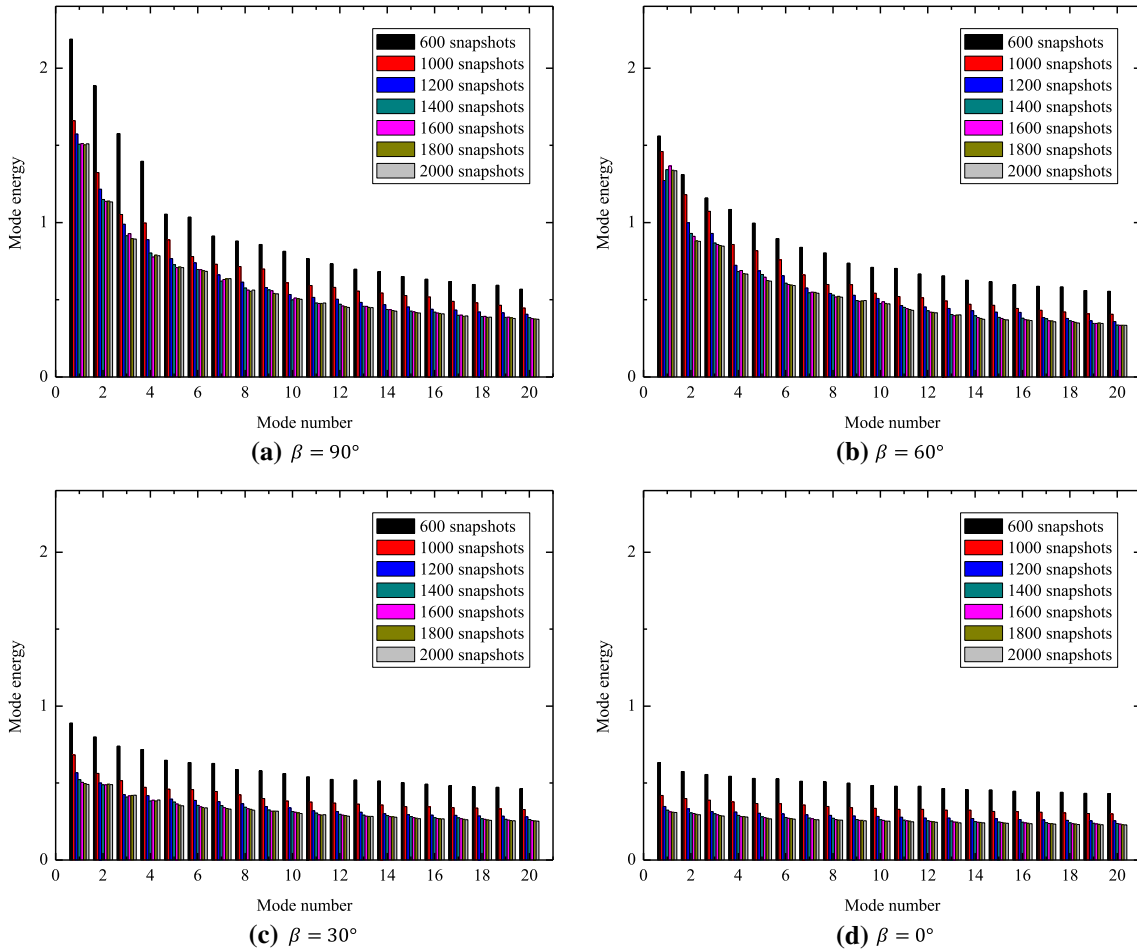
Figure 14 depicts the four most energetic POD modes plotted as sectional streamlines and in-plane velocity contours for the corrugated duct at the downstream station  $z/D = 2$ . As can be seen, some interesting information can be obtained from these results. First, as for relatively large bend angle (i.e.,  $\beta = 90^\circ$  or  $60^\circ$ ), the first mode exhibits a single cell spanning the whole cross section with its center close to the inner wall of the duct. This is found to inherit the most turbulent energy of the Dean cells (Fig. 13). However, as for relatively small bend angle (i.e.,  $\beta = 30^\circ$  or  $0^\circ$ ), the first mode seems to be largely weakened together with the emerging of small-scale vortices. Second, as the mode number increases, the scale of the mode vortices for the bent duct is found to be significantly reduced, which is also accompanied by the forming of small-scale vortices. This could be, to some extent, regarded as a general mark of turbulent energy decay with respect to the Dean cells. Third, the first four POD modes of the corrugated duct (i.e.,  $\beta = 90^\circ, 60^\circ, 30^\circ$ ) exhibit relatively large-scale and well-organized flow structures, whereas the straight corrugated duct (i.e.,  $\beta = 0^\circ$ ) shows small-scale and wide-spread ones. This seems to reveal the underlying flow mode patterns concerned with the developing of the Dean cells.

Figure 15 and Supplementary Movie 3 show the flow field reconstruction of the most energetic POD mode (i.e., the first mode) for the corrugated duct at the downstream station  $z/D = 2$ . Apparently, the most energetic POD mode is found to induce the forming of the classic Dean cells for the bent duct rather than the straight one. Meanwhile, as time marches, these Dean cells start to exhibit a typical dynamic behavior, i.e., the swirl switching [16]: the flow switches in a somewhat erratic fashion between two bistable states where either vortex dominates over the other. In addition, a larger bend angle can also be found to cause the much stronger Dean cells as observed in Figs. 6, 7 and 10. Figure 16 shows the flow field reconstruction of the first  $N$  POD modes covering 20% of the turbulent kinetic energy (TKE). In this case, the flow possesses larger portion of the original turbulent energy as compared to that of Fig. 15, thus exhibiting much stronger Dean cells. However, the major dynamic behavior (i.e., swirl switching) of the flow structure (i.e., Dean cell) tends to get more ambiguous with more low-energy POD modes employed to reconstruct the flow field. This means that these low-energy POD modes are expected to obscure the main energetic features of high-energy POD modes when



**Fig. 16** The flow reconstruction of the first  $N$  POD modes covering 20% of the turbulent kinetic energy (TKE) in cross sections at  $z/D = 2$  under various bend angles: **a**  $\beta = 90^\circ$ ; **b**  $\beta = 60^\circ$ ; **c**  $\beta = 30^\circ$ ; **d**  $\beta = 0^\circ$

intruding into the flow field. Hence, the swirl switching behavior appears to be somewhat damped due to the intrusion of low-energy POD modes (Supplementary Movie 3).



**Fig. 17** POD mode energy (TKE) distribution with various numbers of snapshots and bend angles in the longitudinal section ( $y = 0$ ): **a**  $\beta = 90^\circ$ ; **b**  $\beta = 60^\circ$ ; **c**  $\beta = 30^\circ$ ; **d**  $\beta = 0^\circ$

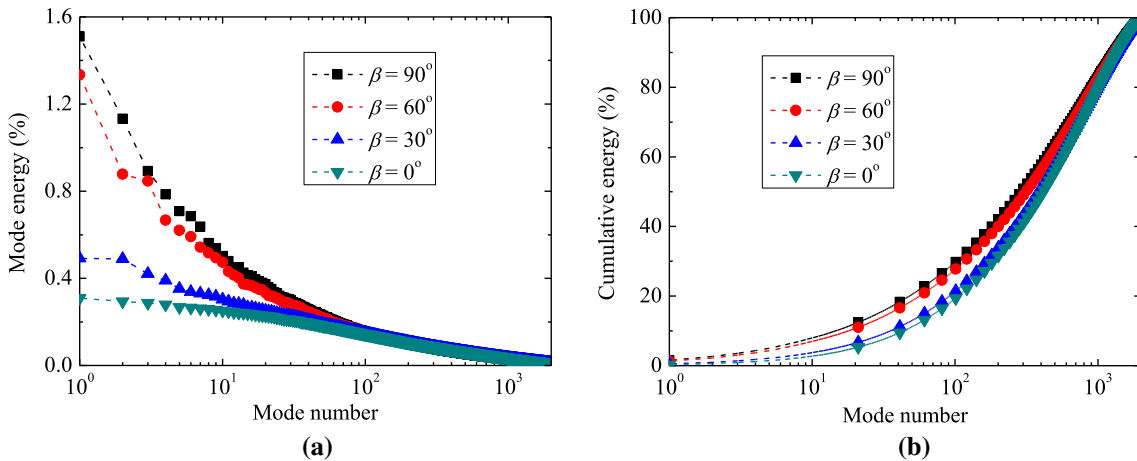


**Fig. 18** **a** Scaled mode energy and **b** cumulative (integrated) mode energy distributions in longitudinal sections (plane at  $y/D = 0$ ) under various bend angles



In order to further understand the flow structure evolution in the streamwise direction, the POD analysis is also performed in longitudinal sections for each duct. Figure 17 shows the effect of the number of snapshots on the POD mode with respect to the mode energy (i.e., TKE) distributions for the first twenty modes in the longitudinal section (i.e., plane at  $y = 0$ ) with various bend angles. As can be seen, there is little visually detectable change in the mode energy distribution of each duct when the number of snapshots increases from 1500 to 2000. Therefore, the present work applies 2000 snapshots to extract the spatial modes in the longitudinal section. Figure 18 shows the individual and cumulative mode energy distributions in longitudinal sections (i.e., plane at  $y = 0$ ) for the corrugated duct with various bend angles. As it is observed in cross sections (Fig. 13), the first few modes also occupy larger portion of fluctuating energy of the original flow field, while they appear to exhibit a milder decay with the increase in the mode number as compared to that in cross sections. This implies that the flow structures in longitudinal sections are supposed to contain a wider range of turbulent scales. Meanwhile, like the findings in cross sections (Fig. 13), an increase in bend angle is also found to boost the inheritance of the turbulent energy for the first few POD modes.

Figure 19 depicts the four most energetic POD modes plotted as normal velocity ( $u_n$ ) component in longitudinal sections for the corrugated duct with various bend angles. It can be observed that the bent corrugated duct seems to present wave-like structures, which survive from the remnant of preexisting flow structures formed in the bent sections. However, no such structures can be found in the straight corrugated duct. This further indicates that the duct bend is supposed to induce the large-scale turbulent structures pertinent to the

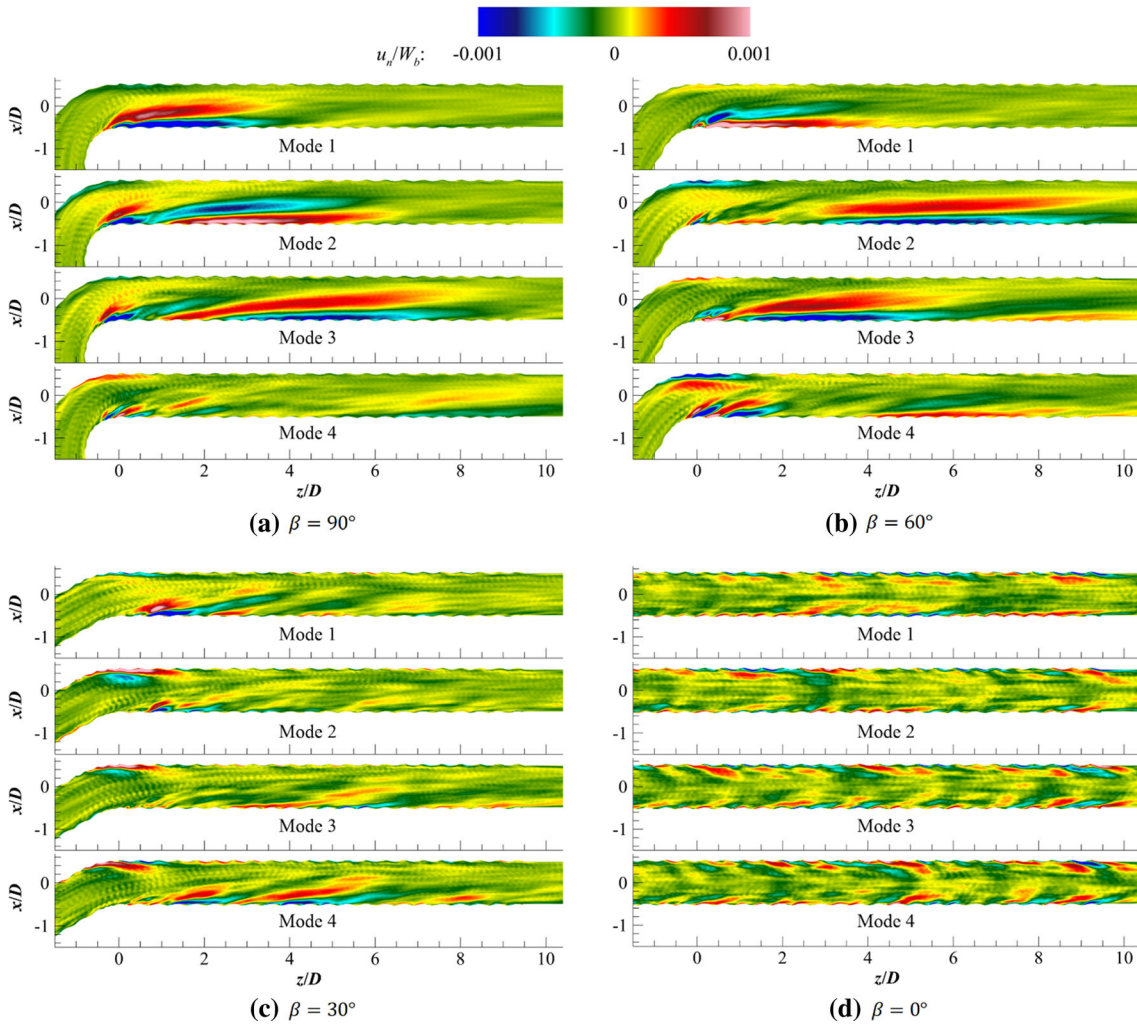


**Fig. 19** The first four POD modes plotted as normal velocity ( $u_n$ ) component in longitudinal sections (plane at  $y/D = 0$ ) under various bend angles: **a**  $\beta = 90^\circ$ ; **b**  $\beta = 60^\circ$ ; **c**  $\beta = 30^\circ$ ; **d**  $\beta = 0^\circ$

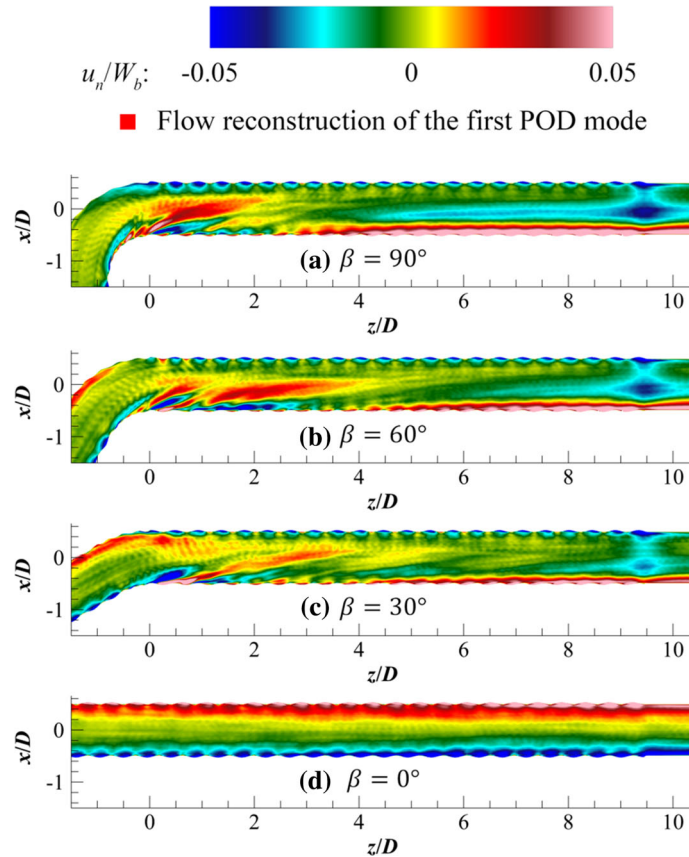


**Fig. 20** The flow reconstruction of the first POD mode in longitudinal sections (plane at  $y/D = 0$ ) under various bend angles: **a**  $\beta = 90^\circ$ ; **b**  $\beta = 60^\circ$ ; **c**  $\beta = 30^\circ$ ; **d**  $\beta = 0^\circ$

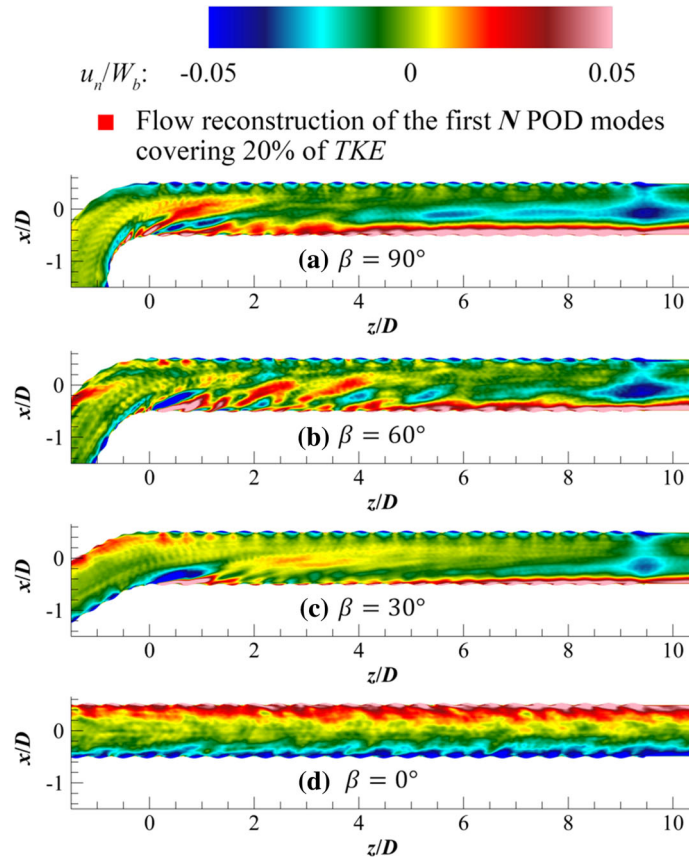
forming of Dean cells. Moreover, as it is anticipated, the POD modes of larger bend angle exhibit larger-scale structures corresponding to higher inheritance of turbulent energy (Fig. 18).

Figure 20 and Supplementary Movie 4 show the flow field reconstruction of the most energetic POD mode (i.e., the first mode) in longitudinal sections for the corrugated duct with various bend angles. As for the bent duct, the first POD mode is found to initiate the forming of wave-like structures, which is expected to mainly modulate the streamwise advection of the Dean cells. However, this most energetic POD mode of the straight duct seems to only play a limited role in modulating the turbulent instability within the boundary layer. Combined with the aforementioned POD analysis in cross sections (Fig. 15), it can be concluded that a larger bend angle tends to create larger-scale structures originating from the bend in a longitudinal section (Fig. 20), which is deemed to play a critical role in modulating the swirl-switching and streamwise advection of the corresponding Dean cells. Figure 21 shows the flow field reconstruction of the first  $N$  POD modes covering 20% of the turbulent kinetic energy (TKE). In this case, the flow starts to occupy larger portion of the original turbulent energy as compared to that of Fig. 20, thus exhibiting stronger and multi-scale wave-like structures. In addition, as it is expected, the largest bend angle is found to cause the strongest waves due to the highest swirl intensity developing within the bend. This could be expected to provide underlying flow physics for potential flow control with respect to the pressure loss reduction in the bent corrugated duct.

## 5 Conclusions

In this work, the effect of bend angle on pressure drop and flow behavior in a small-diameter (i.e., 1 in.) corrugated duct is numerically investigated and experimentally validated under a fully developed flow condition. The large eddy simulation (LES), together with the POD method, is employed to study the pressure drop, mean flow pattern and unsteady flow evolution for the corrugated duct with various bend angles (i.e.,





**Fig. 21** The flow reconstruction of the first  $N$  POD modes covering 20% of the turbulent kinetic energy (TKE) in longitudinal sections (plane at  $y/D = 0$ ) under various bend angles: **a**  $\beta = 90^\circ$ ; **b**  $\beta = 60^\circ$ ; **c**  $\beta = 30^\circ$ ; **d**  $\beta = 0^\circ$

$\beta = 0^\circ, 30^\circ, 60^\circ, 90^\circ$ ). For the experimental validation, an open-circuit low-speed wind tunnel was designed and fabricated to test the typical pressure drop of the corrugated duct with varying bend angles. The results show that the pressure drop of the corrugated duct exhibits a monotonic increase with increasing bend angle. Specifically, as the bend angle increases from  $0^\circ$  to  $90^\circ$ , the pressure drop of the corrugated duct experiences a striking increase of about 43%. Accordingly, a larger bend angle is found to induce the occurrence of stronger Dean cells or larger swirl intensity downstream the duct bend. Meanwhile, as for larger bend angles, the main turbulent properties of the Dean cells could be, to some extent, governed by the first few POD modes, which appear to be featured with one or few large-scale vortices. In addition, these Dean cells are found to be advected downstream by a series of wave-like structures. Generally, the larger bend angle causes stronger swirl intensity and wave-like structures, thus rendering severer pressure drop or larger pressure loss coefficient in the corrugated duct.

The present study provides the fundamental flow behavior as well as the corresponding pressure loss pertinent to the airflow passing through the corrugated duct with various bend angles, which can be expected to increase the design knowledge base for the bent corrugated duct installation and maintenance for commercial buildings. In addition, the proper knowledge of the fundamental flow evolution and pressure loss pattern within the bent corrugated duct is also supposed to provide potential design guidelines for energy saving of the HVAC system ductwork. On the other hand, in many other engineering applications, such as dedusting and demisting in process, oil and gas industries, the particle and droplet deposition in turbulent-swirled flow [19] potentially occurring within corrugated ducts is also recommended to be investigated in future studies.

**Acknowledgements** This work is supported by Open Fund of Key Laboratory of Icing and Anti/De-icing of Aircraft (Grant No.: AIADL20180102), International Frontier-Interdisciplinary Key Projects of Tongji University (Grant No.: 2019010108), and Fundamental Research Funds for the Central Universities (Grant No.: 22120190286).

### Compliance with ethical standards

**Conflict of interest** None.

### References

- Fisk, W.J., Delp, W., Diamond, R., Dickerhoff, D., Levinson, R., Modera, M., et al.: Duct systems in large commercial buildings: physical characterization, air leakage, and heat conduction gains. *Energy Build.* **32**(1), 109–119 (2000)
- Cantrill, D.L.: Static Pressure Loss in 12", 14", and 16" Non-metallic Flexible Duct. Doctoral dissertation (2013)
- Krishnamoorthy, S., Modera, M., Harrington, C.: Efficiency optimization of a variable-capacity/variable-blower-speed residential heat-pump system with ductwork. *Energy Build.* **150**, 294–306 (2017)
- Stephens, B.: The impacts of duct design on life cycle costs of central residential heating and air-conditioning systems. *Energy Build.* **82**, 563–579 (2014)
- Manuel, M.C.E., Lin, P.T., Chang, M.: Optimal duct layout for HVAC using topology optimization. *Sci. Technol. Built Environ.* **24**(3), 212–219 (2018)
- Kokayko, M., Holton, J., Beggs, T., Walthour, S., Dickson, B.: Residential ductwork and plenum box bench tests. *IBACOS Burt Hill Proj.* **95006**, 13 (1996)
- Abushakra, B., Walker, I.S., Sherman, M.H.: Compression effects on pressure loss in flexible HVAC ducts. *HVAC&R Res.* **10**(3), 275–289 (2004)
- Handbook, A.F.: American Society of Heating, Refrigerating and Air-Conditioning Engineers. Inc., Atlanta (2009)
- ACCA: Residential Duct Systems. Manual D. Air Conditioning Contractors of America, Washington (2009)
- Ugursal, A., Culp, C.: Comparative analysis of CFD [DELTA] P vs. measured [DELTA] P for compressed flexible ducts. *ASHRAE Trans.* **113**, 462 (2007)
- Jaiman, R.K., Oakley, O.H., Adkins, J.D.: CFD modeling of corrugated flexible pipe. In: ASME 2010 29th International Conference on Ocean, Offshore and Arctic Engineering, pp. 661–670. American Society of Mechanical Engineers Digital Collection (2010)
- Weaver, K.D.: Determining Pressure Losses For Airflow in Residential Ductwork. Doctoral dissertation, MSc. Thesis, Mechanical Eng. Dept., Texas A&M University (2011)
- Liu, R., Wen, J., Waring, M.S.: Improving airflow measurement accuracy in VAV terminal units using flow conditioners. *Build. Environ.* **71**, 81–94 (2014)
- Liu, R., Wen, J., Zhou, X., Klaassen, C.: Stability and accuracy of variable air volume box control at low flows. Part 1: laboratory test setup and variable air volume sensor test. *HVAC&R Res.* **20**(1), 3–18 (2014)
- Hellström, L.H., Zlatinov, M.B., Cao, G., Smits, A.J.: Turbulent pipe flow downstream of a 90° bend. *J. Fluid Mech.* **735** (2013)
- Kalpikli Vester, A., Örlü, R., Alfredsson, P.H.: Turbulent flows in curved pipes: recent advances in experiments and simulations. *Appl. Mech. Rev.* **68**(5) (2016)
- Wang, Z., Örlü, R., Schlatter, P., Chung, Y.M.: Direct numerical simulation of a turbulent 90° bend pipe flow. *Int. J. Heat Fluid Flow* **73**, 199–208 (2018)
- Kulkarni, D., Idem, S.: Loss coefficients of bends in fully stretched nonmetallic flexible ducts. *Sci. Technol. Built Environ.* **21**(4), 413–419 (2015)
- Zonta, F., Marchioli, C., Soldati, A.: Particle and droplet deposition in turbulent swirled pipe flow. *Int. J. Multiph. Flow* **56**, 172–183 (2013)
- Weaver, K., Charles Culp, P.E.: Static pressure losses in nonmetallic flexible duct. *ASHRAE Trans.* **113**, 400 (2007)
- Haug, J.P., Rademakers, R.P., Stöbel, M., Niehuis, R.: Numerical flow field analysis in a highly bent intake duct. In: ASME Turbo Expo 2018: Turbomachinery Technical Conference and Exposition. American Society of Mechanical Engineers Digital Collection (2018)
- Moujaes, S.F., Aekula, S.: CFD predictions and experimental comparisons of pressure drop effects of turning vanes in 90 duct elbows. *J. Energy Eng.* **135**(4), 119–126 (2009)
- Shirzadi, M., Mirzaei, P.A., Naghashadegan, M.: Development of an adaptive discharge coefficient to improve the accuracy of cross-ventilation airflow calculation in building energy simulation tools. *Build. Environ.* **127**, 277–290 (2018)
- Du, X., Yang, Z., Jin, Z., Xia, C., Bao, D.: A comparative study of passive control on flow structure evolution and convective heat transfer enhancement for impinging jet. *Int. J. Heat Mass Transf.* **126**, 256–280 (2018)
- Germano, M., Piomelli, U., Moin, P., Cabot, W.H.: A dynamic subgrid-scale eddy viscosity model. *Phys. Fluid A* **3**(7), 1760–1765 (1991)
- Smagorinsky, J.: General circulation experiments with the primitive equations: I. The basic experiment. *Month. Weather Rev.* **91**(3), 99–164 (1963)
- Lilly, D.K.: A proposed modification of the Germano subgrid-scale closure method. *Phys. Fluids A: Fluid Dyn.* **4**(3), 633–635 (1992)
- Hinze, J.O.: Turbulence. McGraw-Hill Publishing Co., New York (1975)
- Aldrich, R., Puttagunta, S.: Measure Guideline: Sealing and Insulating of Ducts in Existing Homes (No. DOE/GO-102011-3474). National Renewable Energy Lab. (NREL), Golden (2011)
- Leonard, B.P.: A stable and accurate convective modelling procedure based on quadratic upstream interpolation. *Comput. Methods Appl. Mech. Eng.* **19**(1), 59–98 (1979)

31. Leonard, B.P.: Simple high-accuracy resolution program for convective modelling of discontinuities. *Int. J. Numer. Methods Fluids* **8**(10), 1291–1318 (1988)
32. Moffat, R.J.: Describing the uncertainties in experimental results. *Exp. Therm. Fluid Sci.* **1**(1), 3–17 (1988)
33. Gupta, A.K., Lilley, D.G., Syred, N.: *Swirl Flows*. Tunbridge Wells, Kent, England, Abacus Press, Kent (1984)
34. Sirovich, L.: Turbulence and the dynamics of coherent structures. I. Coherent structures. *Quart. Appl. Math.* **45**(3), 561–571 (1987)
35. Loeve, M.: *Probability Theory: Foundations, Random Sequences*. van Nostrand, Princeton (1955)
36. Lumley, J.L.: The structure of inhomogeneous turbulent flows. In: Yaglom, A.M., Tartarsky, V.I. (eds.) *Atmospheric Turbulence and Radio Wave Propagation*, pp. 166–178. Nauka, Moscow (1967)
37. Taira, K., Brunton, S.L., Dawson, S.T.M., Rowley, C.W., Colonius, T., McKeon, B.J., et al.: Modal analysis of fluid flows: an overview. *AIAA J.* 4013–4041 (2017)
38. Holmes, P., Lumley, J.L., Berkooz, G.: *Coherent Structures, Dynamical Systems and Symmetry*. Cambridge University Press, Cambridge (1996)
39. Gamard, S., George, W.K., Jung, D., Woodward, S.: Application of a “slice” proper orthogonal decomposition to the far field of an axisymmetric turbulent jet. *Phys. Fluids* **14**(7), 2515–2522 (2002)
40. Eckart, C., Young, G.: The approximation of one matrix by another of lower rank. *Psychometrika* **1**(3), 211–218 (1936)

**Publisher's Note** Springer Nature remains neutral with regard to jurisdictional claims in published maps and institutional affiliations.